Cell Calcium 100 (2021) 102494

Contents lists available at ScienceDirect

Cell Calcium

journal homepage: www.elsevier.com/locate/ceca

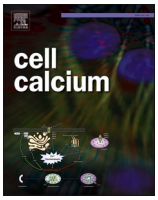

Termination of Ca^{2+} puffs during IP_3-evoked global Ca^{2+} signals

Jeffrey T. Lock [a,*], Ian Parker [a,b]

[a] Department of Neurobiology & Behavior, UC Irvine, Irvine, CA United States
[b] Department of Physiology & Biophysics, UC Irvine, Irvine, CA United States

ARTICLE INFO

Keywords:
IP_3 receptor
IP_3 signaling
Calcium signaling
Ca^{2+} puffs
Calcium imaging

ABSTRACT

We previously described that cell-wide cytosolic Ca^{2+} transients evoked by inositol trisphosphate (IP_3) are generated by two modes of Ca^{2+} liberation from the ER; 'punctate' release via an initial flurry of transient Ca^{2+} puffs from local clusters of IP_3 receptors, succeeded by a spatially and temporally 'diffuse' Ca^{2+} liberation. Those findings were derived using statistical fluctuation analysis to monitor puff activity which is otherwise masked as global Ca^{2+} levels rise. Here, we devised imaging approaches to resolve individual puffs during global Ca^{2+} elevations to better investigate the mechanisms terminating the puff flurry. We find that puffs contribute about 40% (~90 attomoles) of the total Ca^{2+} liberation, largely while the global Ca^{2+} signal rises halfway to its peak. The major factor terminating punctate Ca^{2+} release is an abrupt decline in puff frequency. Although the amplitudes of large puffs fall during the flurry, the amplitudes of more numerous small puffs remain steady, so overall puff amplitudes decline only modestly (~30%). The Ca^{2+} flux through individual IP_3 receptor/channels does not measurably decline during the flurry, or when puff activity is depressed by pharmacological lowering of Ca^{2+} levels in the ER lumen, indicating that the termination of punctate release is not a simple consequence of reduced driving force for Ca^{2+} liberation. We propose instead that the gating of IP_3 receptors at puff sites is modulated such that their openings become suppressed as the bulk $[Ca^{2+}]$ in the ER lumen falls during global Ca^{2+} signals.

1. Introduction

Cytosolic Ca^{2+} signals generated by the liberation of Ca^{2+} ions sequestered in the endoplasmic reticulum (ER) through inositol trisphosphate receptor (IP_3R) channels regulate ubiquitous cellular processes as diverse as gene transcription, secretion, mitochondrial energetics, electrical excitability and fertilization [1, 2]. Such unique repertories of Ca^{2+}dependent functions are achieved through a hierarchy of cytosolic Ca^{2+} signals with markedly different spatial scales and temporal durations, ranging from transient, subcellular Ca^{2+} signals called puffs [3–5] to more prolonged global Ca^{2+} elevations that engulf the cell [6]. This patterning is shaped by the functional properties of IP_3Rs together with their spatial arrangement in the cell. Biphasic modulation of IP_3R channel gating by cytosolic Ca^{2+}results in a phenomenon of Ca^{2+}-induced Ca^{2+}-release (CICR) [7, 8]. Ca^{2+} diffusing from one open channel may thus trigger the opening of adjacent channels, with self-reinforcing CICR countered by inhibitory feedback at high $[Ca^{2+}]$. The clustered distribution of IP_3Rs further defines the extent of this regenerative process as puffs arise from localized CICR between IP_3Rs within stationary clusters, where they are preferentially 'licensed' to respond [4, 9]. A widely-accepted model further posits that global Ca^{2+}signals arise through successive recruitment of puffs via cycles of CICR and Ca^{2+} diffusion between the IP_3R clusters at puff sites – in essence, that puffs are the basic 'building block' from which all IP_3-mediated cellular Ca^{2+}signals are constructed [5, 10–15].

We recently challenged that notion [16], utilizing a statistical technique of fluctuation analysis of Ca^{2+}imaging data to monitor bulk puff activity during global responses, even when individual puffs were obscured by large cell-wide Ca^{2+}elevations. We found that although a flurry of puff activity was prominent during the initial portion of the global Ca^{2+}response and peaked early during the rising phase, it then terminated around the midpoint of the rising phase. Notably, global Ca^{2+} levels continued to climb after puffs had largely ceased, and cytosolic Ca^{2+} remained elevated for several seconds following the apex of the global signal, during which time local Ca^{2+} fluctuations were substantially suppressed. The flurry of puffs did not cease because IP_3Rs became inhibited by the rising cytosolic Ca^{2+}levels during the spike, but instead appeared to terminate because of falling levels of Ca^{2+} in the ER

* Corresponding author at: Department of Neurobiology and Behavior University of California, Irvine, CA 92697 United States.
E-mail address: lockj@uci.edu (J.T. Lock).

https://doi.org/10.1016/j.ceca.2021.102494
Received 31 August 2021; Received in revised form 12 October 2021; Accepted 13 October 2021
Available online 21 October 2021

lumen [16]. Indeed, by prior partial depletion of ER Ca^{2+}we were able to evoke global Ca^{2+}responses in the absence of puffs. We thus proposed the existence of two distinct modes of IP_3-mediated Ca^{2+}liberation: 'punctate' liberation in the form of transient, local Ca^{2+}puffs, and a second 'diffuse' mode of liberation that is more homogeneous in space and time [16].

Although our fluctuation analysis technique provided a gross measure of puff activity across the cell it did not resolve individual puffs, leaving important questions unanswered. How is the termination of the puff flurry reflected in the behavior of individual puff sites? Does the decline in punctate Ca^{2+}liberation arise simply because of reduced driving force as ER levels decline, or is the gating of IP_3Rs modulated? Here, we address these issues by applying experimental and image-processing techniques that enable the resolution of individual puffs during the rise of global Ca^{2+}signals.

2. Materials and methods

2.1. Cells and cell-loading

HEK293 wild-type cells were kindly provided by Dr. David Yule (University of Rochester) and were cultured in Eagle's Minimum Essential Medium (EMEM; ATCC #30–2003), supplemented with 10% fetal bovine serum (Omega Scientific #FB-11). Cells were grown in plastic 75 cm flasks and maintained at 37 °C in a humidified incubator gassed with 95% air and 5% CO_2. For imaging, cells were collected using 0.25% Trypsin-EDTA (ThermoFisher #25,200–056) and grown on poly-D-lysine coated (1 mg/ml; Sigma #P0899) 35-mm glass bottom imaging dishes (MatTek #P35–1.5–14-C).

Cells were incubated with the membrane-permeant fluorescent Ca^{2+} indicator Cal520/AM (1–5 μM; AAT Bioquest #21,130) for 1 hr at room temperature in a Ca^{2+}-containing HEPES buffered salt solution (Ca^{2+}-HBSS) together with membrane permeant ester of the caged IP_3 analogue ci-IP_3/PM [D-2,3,-O-Isopropylidene-6-O-(2-nitro-4,5 dimethoxy) benzyl-myo-Inositol 1,4,5,-trisphosphate hexakis (propionoxymethyl) ester] (1 μM; SiChem #cag-iso2–145–10). Except where indicated, cells were additionally loaded by incubation with EGTA/AM (15 μM; Thermo Fisher Scientific #E1219) for a further 1 hr at room temperature in Ca^{2+}-HBSS to attenuate global Ca^{2+} elevations. Cells were finally maintained for 30 min at room temperature in Ca^{2+}-HBSS before imaging. The genetically encoded, ER-targeted Ca^{2+} indicator R-$CEPIA_{ER}$ [17] was transfected into cells using lipofectamine 3000 (ThermoFisher #L3000008) according to the manufacturer's instructions, and imaged 24–48 hrs later. Cal520/AM, i-IP_3/PM, and EGTA/AM were all solubilized with DMSO/20% pluronic F127 (ThermoFisher #P3000MP). Carbachol (CCH; #C4382) and cyclopiazonic acid (CPA; #C1530) were purchased from Sigma and dissolved in deionized water and 100% ethanol, respectively. Ca^{2+}-HBSS contained (in mM) 135 NaCl, 5.4 KCl, 2 $CaCl_2$, 1 $MgCl_2$, 10 HEPES, and 10 glucose (pH=7.4). Ca^{2+}-free HBSS consisted of the same formulation except that $CaCl_2$ was omitted and 300 μM EGTA was added.

2.2. Microscopy

Total internal reflection fluorescence (TIRF) imaging of Ca^{2+} signals was accomplished using a home-built microscope system, based around an Olympus (Center Valley, PA) IX50 microscope equipped with an Olympus 60X oil immersion TIRF objective (NA 1.45), and an Evolve EMCCD camera (Photometrics; Tucson, AZ) with a bit depth of 16 bits, using 2 × 2 binning for a final field at the specimen of 128 × 128 binned pixels (one binned pixel = 0.53 μm) at rates of 125 or 227 frames s^{-1}. All references to 'pixel' in this paper refer to the binned pixel. Image data were streamed to computer memory using Metamorph v7.7 (Molecular Devices; San Jose, CA) and stored on hard disk for offline analysis. Cal520 fluorescence was excited using a 488 nm laser and detected through a 510 nm long-pass (LP) emission filter; R-CEPIAer imaging utilized a 561 nm excitation laser and a 568 nm LP emission filter. Photorelease of i-IP_3 was evoked by UV light from a xenon arc lamp filtered through a 350–400 nm bandpass filter and introduced by a UV-reflecting dichroic in the light path to uniformly illuminate the field of view. The amount of i-IP_3 released was controlled by varying the flash duration by an electronically controlled shutter. Carbachol was locally applied to cells through glass micropipettes with tip diameters of ~1–2 μm using a pneumatic picospritzer. All imaging was performed at room temperature while cells were bathed in zero Ca^{2+}-HBSS containing 0.3 mM EGTA and no added Ca^{2+}.

2.3. Image processing

Image data in 16 bit integer multi-plane TIF format were imported into FLIKA (http://flika-org.github.io), a freely available open-source image processing and analysis software in the Python programming language [18,19]. Internal processing and data output were performed using 64 bit floating-point arithmetic. Processing was performed on image stacks following subtraction of camera black offset level (500 camera units). F/F_0 ratio stacks were generated by dividing each frame in the offset-corrected raw image stack by an average of 100 baseline frames acquired before stimulation. $\Delta F/F_0$ image stacks were generated by subtracting 1 from F/F_0 ratio stacks.

To derive image stacks representing the pixel-by-pixel standard deviation (SD) of temporal fluctuations in fluorescence of the Ca^{2+} indicator dye we used a custom FLIKA script as described previously [16,19]. In brief, following subtraction of camera black offset level, the raw image stack from the camera was first spatially filtered by a Gaussian blur function with a standard deviation (sigma) of 2 pixels (~1 μm at the specimen). To attenuate high-frequency photon shot noise and low frequency changes in baseline fluorescence, stacks were temporally filtered by a bandpass Butterworth filter with low and high cutoff frequencies of 3 and 20 Hz. A running variance of this temporally filtered movie was calculated, pixel by pixel, by subtracting the square of the mean from the mean of the square of a moving 20 frame (160 ms) boxcar window of the movie. The running standard deviation was calculated by taking the square root of the variance image stack to create a standard deviation (SD) stack. Finally, to remove the mean predicted photon shot noise (whose variance increases in linear proportion to the mean fluorescence intensity) the SD stack was corrected, pixel-by-pixel, by subtracting the square root of a running mean of the spatially filtered fluorescence image stack multiplied by a scalar constant derived as described previously [16,19]. Traces showing changes in SD signal throughout Ca^{2+} responses were measured from a region of interest (ROI) encompassing the entire cell or part of the cell within the imaging field, and from small (4 × 4 pixel; 2 × 2 μm) ROIs. The locations of active puff sites were readily visualized by forming maximum intensity SD projection images where the intensity of each pixel is the maximum at that pixel across a range of frames acquired during the rising phase of Ca^{2+} responses.

To enable analysis of fluorescence signals generated by individual puffs we applied a custom FLIKA routine (scaled peak subtraction; SPS) to strip off the slow bulk rise in fluorescence during global Ca^{2+} responses to achieve a substantially flat baseline. This operated by forming an averaged image of frames (usually 100) at the time of peak global response and then subtracting a scaled version of this, frame-by-frame, from the original $\Delta F/F_0$ image stack. The scaling factor was derived as a running mean (usually 20 frames) of the whole-cell fluorescence at each time, expressed as a fraction of the change in $\Delta F/F_0$ from pre-stimulus baseline to the mean peak $\Delta F/F_0$. The resulting image stack was then processed using the 'detect puffs' algorithm in FLIKA to measure peak amplitude, duration (from 20% rise to 80% fall from peak), and integral of each puff (Fig. 2). Measurements of dwell-state amplitudes (Fig. 4) were made by visual inspection of SPS-processed $\Delta F/F_0$ traces from 4 × 4 pixel regions placed on puff sites identified from maximum-intensity projections of SD images.

2.4. Simulations

A custom plugin 'simulate puffs' in FLIKA was used to add synthetic puffs to an imaging record of a CPA-treated HEK cell that produced a global rise in Ca^{2+} fluorescence in response to photoreleased i-IP_3 in the absence of any detectable puff activity [16]. The size and kinetic parameters of simulated events listed in the legends of fig. S5 and fig. S6 were chosen to approximate experimental observations of small Ca^{2+} puffs and single-channel blips [20–22]. Simulations were then processed in the manner described above for automated and visual analysis of experimental Ca^{2+} imaging records.

2.5. Statistics

Mean values are expressed throughout as standardized means ± 1 SEM, where n is the number of cells analyzed. Comparison of mean values between two groups was assessed by both Student's T-test (parametric) and Mann-Whitney test (nonparametric). Differences were considered statistically significant when indicated by both parametric and nonparametric approaches; the larger of the two P values are presented throughout. Statistical significance in figures is denoted as $*P < 0.05$ and $**P < 0.01$.

3. Results

3.1. Techniques to improve resolution of Ca^{2+} puffs during global Ca^{2+} responses

Localized, Ca^{2+}transients (puffs) are observed during the rising phase of IP_3-evoked global (cell-wide) cytosolic Ca^{2+}responses in many cell types[10–16]. Because the puffs become difficult to resolve as the global fluorescence Ca^{2+} signal increases, we previously developed image processing and analysis routines to display and analyze local fluctuations in Ca^{2+} fluorescence signals [16,19]. That procedure is illustrated in Fig. 1A,B. The top panels in Fig. 1A show 'snapshots' of fluorescence ratio signals ($\Delta F/F_0$) imaged by TIRF microscopy of an HEK cell loaded with the Ca^{2+} indicator Cal520 at different times during the rise of a global Ca^{2+} signal evoked by photorelease of i-IP_3 from a caged precursor. Localized puffs can be discerned as increases in Cal520 $\Delta F/F_0$ in the first three top panels of Fig. 1A, but are more apparent in the middle panels that show corresponding SD images depicting a running time-average of the standard deviation of Ca^{2+}-dependent fluctuations in fluorescence. Fig. 1B shows measurements from the same cell of the global (cell-wide) Ca^{2+} signal (smooth black trace; Cal520 $\Delta F/F_0$) and global SD signal (noisy red trace). Measurements of global SD signals provide a population average of Ca^{2+}fluctuations associated with puff activity at multiple sites across the cell [16], and measurement of fluctuations from small ROIs at active sites reveal the activity of individual puffs (Fig. 1C).

However, although SD fluctuation measurements identify puffs with a better signal-to-noise ratio than the underlying fluorescence signal, they are not optimal to determine the properties of individual puffs because the magnitude of the SD signal is a function of both the amplitude and kinetics of the Ca^{2+} fluorescence signal ($\Delta F/F_0$), and its time course is constrained by the duration (typically 20 frames, 160 ms) of the running boxcar window over which the standard deviation is calculated. We thus devised two approaches that, in combination, enable enhanced resolution of Ca^{2+}puffs while flattening the baseline on which they are superimposed. First, to flatten the baseline we stripped off the global rise in bulk fluorescence, using an algorithm to subtract from each frame of the $\Delta F/F_0$ image stack an average image of frames acquired around the peak of the response that was scaled in proportion to the global fluorescence of the cell at each time. This procedure (scaled peak subtraction; 'SPS') substantially flattened the baseline, but alone could not entirely compensate for spatial inhomogeneities in Ca^{2+} during the global response (lower panels of Fig. 1A; Fig. 1D). Moreover, the increased photon shot noise resulting from the increase in fluorescence impaired the resolution of puffs during later phases of the response.

We thus applied a complimentary experimental approach to mitigate these effects, based on cytosolic loading of EGTA. This slow Ca^{2+}buffer selectively diminishes global baseline Ca^{2+} elevations evoked by IP_3 [27–29], while having little effect on the amplitude of the transient fluorescence signals from puffs (fig. S1), 'sharpening' them in space and time so they become more localized and display kinetics that closely track the openings and closings of individual IP_3R channels [22,29,30]. Figs. 1E-H illustrate representative records, processed and displayed in the same way as for the cell in Fig. 1A-D, but from a cell loaded with EGTA by prior incubation with 15 μM EGTA/AM for 1 hr; a protocol chosen to substantially reduce the peak amplitude of the global signal while minimally affecting the SD signal reflecting puff activity. As illustrated in Fig. 1H, the combination of EGTA-loading and SPS image processing to strip the bulk global rise in Ca^{2+} signal enabled recordings on which individual puffs were readily resolved on a stable, flat baseline, and with reduced photon shot noise because the overall fluorescence increase was smaller.

A possible concern with using EGTA to reduce the amplitude of global Ca^{2+} elevations was that, beyond buffering the rise in cytosolic free Ca^{2+}, it might depress the Ca^{2+} release process by impairing CICR between IP_3Rs. To discriminate between these possibilities we monitored ER Ca^{2+} levels during global responses evoked by bath application of carbachol (CCH; 100 μM) using the ER-targeted, low-affinity Ca^{2+} sensor R-CEPIA$_{ER}$ [17]. EGTA-loaded cells showed a larger drop and slower refilling of ER Ca^{2+} (fig. S2A), mirroring the reduced amplitude and slowed falling phase of cytosolic Ca^{2+} signals (fig. S2B). The reduced amplitude of the global cytosolic Cal520 signal is readily explained by the action of EGTA to buffer free Ca^{2+} ions. Further, the greater fall in ER Ca^{2+} level indicates that Ca^{2+} release was actually potentiated (fig. S2C), likely because the reduced rise in free cytosolic Ca^{2+} both increased the concentration gradient for Ca^{2+} efflux from the ER and reduced inhibitory feedback of cytosolic Ca^{2+} on the IP_3R channels. Importantly, despite strongly attenuating the CCH-evoked rise in global cytosolic Ca^{2+} (fig. S2D), the distinct punctate and diffuse modes of Ca^{2+} liberation were preserved after EGTA loading [16] and their temporal relationship was retained, with puff activity declining abruptly as the global response reached about half-way toward its peak (Fig. 1).

Unless otherwise noted, all following results in this paper were obtained in EGTA-loaded HEK cells. Moreover, all experiments were done while cells were bathed in a solution containing no added Ca^{2+} and 300 μM EGTA to exclude Ca^{2+} influx across the plasma membrane, so the responses arise exclusively from Ca^{2+} liberated from intracellular stores.

3.2. Patterns of puff activity during global i-IP_3-evoked responses

Fig. S3 illustrates representative spatio-temporal patterns of puff activity during a global i-IP_3-evoked response in an EGTA-loaded cell, derived using both SD analysis (fig. S3A-D) and SPS processing (fig. S3E, F) of fluorescence signals. Projection images from the SD image stack highlight the locations of multiple hot-spots during the rising phase of the global response (fig. S3A, middle panel), whereas these were absent in images generated from periods before simulation or at the peak of the global response (fig. S3A, left and right panels). Raster plots in fig. S3C,E summarize activity patterns at multiple hot-spots within a single cell displayed, respectively, in terms of local fluctuations (SD signal) and fluorescence ratio signals ($\Delta F/F_0$), throughout the time course of the global Ca^{2+} response. Corresponding traces in fig. S3D,F respectively illustrate SD and $\Delta F/F_0$ signals at five representative sites.

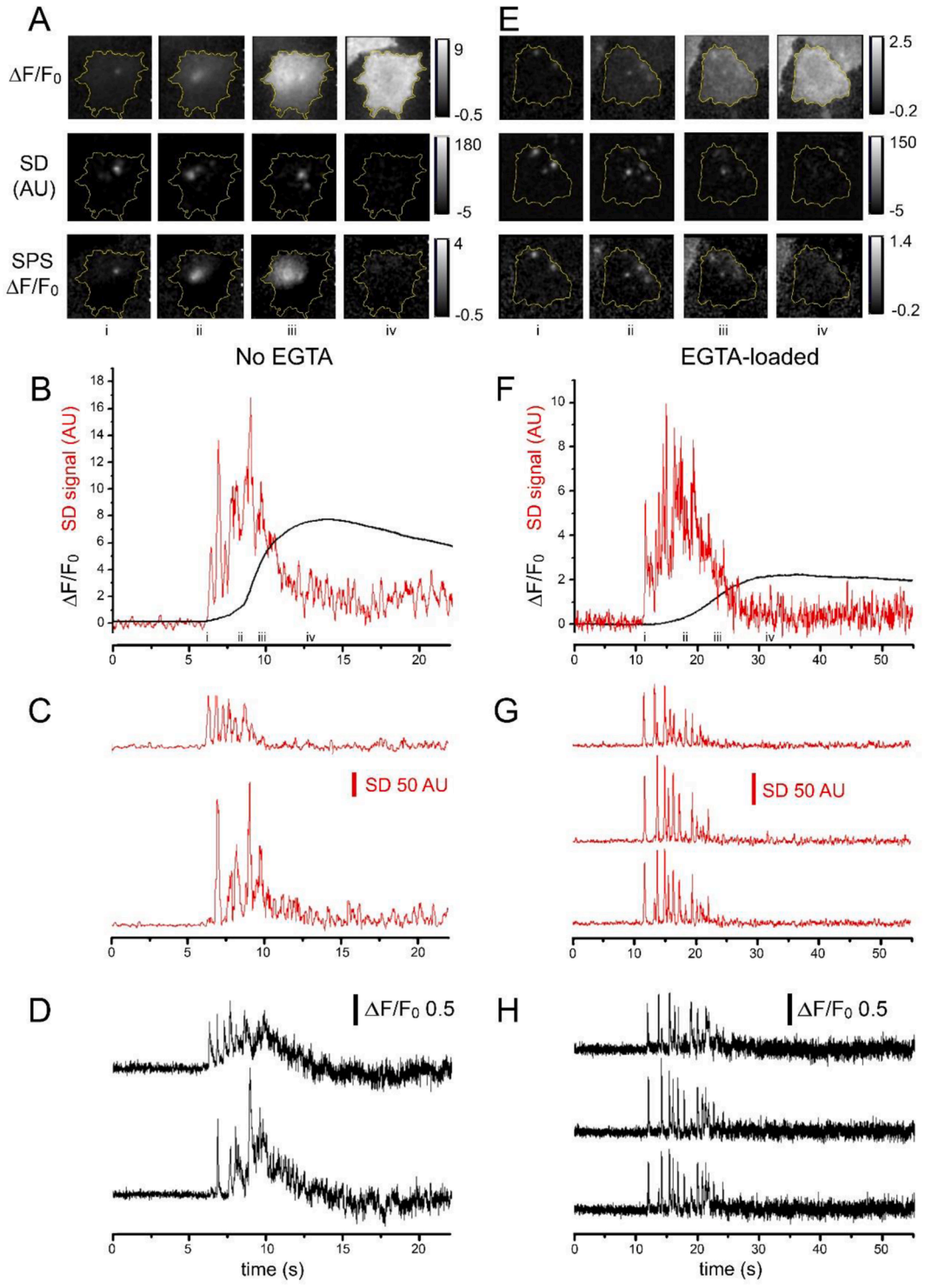

Fig. 1.. Resolution of Ca^{2+} puffs during global IP_3-evoked Ca^{2+} responses. (A-D) Records are from a single WT HEK cell loaded with Cal520 and stimulated by photorelease of i-IP_3 to evoke a global Ca^{2+} elevation. (A) *Upper panels* show TIRF fluorescence ratio ($\Delta F/F_0$) images of the cell at different times (marked by Roman numerals in B) during the rising phase of the global Ca^{2+} signal. Each panel is a single frame snapshot (8 ms exposure). gray scale depicts fluorescence ratio intensities as indicated by the bar on the right. *Middle panels* show corresponding SD images at the same times, with gray scale depicting the temporal standard deviation of fluorescence intensities in arbitrary units. *Lower panels* show corresponding fluorescence ratio ($\Delta F/F_0$) images after processing to strip off the global fluorescence rise, using an algorithm (SPS, scaled peak subtraction) to subtract a scaled version of an averaged image captured at the peak of the response. (B) Traces show measurements from a region of interest (ROI) encompassing the entire cell of the fluorescence ratio signal ($\Delta F/F_0$; smooth black trace) and the SD signal (noisy red trace). (C) Representative traces of SD signals from two small ROIs (4 × 4 pixel; ~2 × 2 μm) centered on puff sites. (D) Fluorescence ratio traces ($\Delta F/F_0$) after SPS processing from the same two ROIs. (E-H) Representative images and traces corresponding to those in A-D, but obtained in a single WT HEK cell that was additionally loaded with EGTA by incubation for 60 min with 15 μM EGTA/AM.

3.3. Changes in puff amplitudes and frequencies during global Ca^{2+} responses

Records like those in fig. S3 portray both a decline in puff amplitudes at some individual sites during the rise of the global Ca^{2+} response, and a marked attenuation in puff frequency and whole-cell SD signal around the time of half-rise to the peak. To quantify these changes we used FLIKA [18,31] to automate detection and measurement of puff parameters (frequency, peak amplitude, duration and integral), after first applying SPS processing to derive $\Delta F/F_0$ image stacks of puffs on a stable baseline fluorescence level. Because the rise time of the global Ca^{2+} signal varies strongly as a function of the amount of photoreleased i-IP_3 [16,32], we separately pooled measurements from four HEK cells that gave relatively 'slow' responses (~50 s from photorelease to peak; Fig. 2, left panels) and from four cells that gave 'fast' responses (~20 s; Fig. 2, right panels). To further compensate for remaining variability in kinetics between the cells in each group (Fig. 2A,H, insets) we plot the data on a normalized time scale, with time $t = 0$ corresponding to the time of the photolysis flash and $t = 1$ corresponding to the time the global fluorescence signal rose to 50% of its peak value for each cell.

Figs. 2A,B show, respectively, overlays of global fluorescence ratio ($\Delta F/F_0$) signals and global SD signals from the four slow-rising cells. Fig. 2C overlays representative puff activity ($\Delta F/F_0$ after SPS processing) at 12 individual sites in a single cell, and histogram bars in Fig. 2D show the total numbers of puffs arising in the four cells during normalized time bins. Notably, about 75% of puffs occurred before the global Ca^{2+} signal had risen to half the peak value (normalized time $t = 1$). Fig. 2E shows a scatter plot of all puff amplitudes (gray symbols) and mean amplitudes at binned intervals (black symbols) throughout the rise of the global responses. Many small amplitude events were observed throughout the course of the global signal, but there was a marked fall-off in large amplitude puffs as Ca^{2+} levels rose, resulting in a 35% reduction in mean puff amplitudes from the start of the puff flurry to the half-rise time in global Ca^{2+} fluorescence. The mean durations of puffs increased slightly throughout the rise of the global Ca^{2+} signal (Fig. 2F), roughly balancing the decline in amplitudes so that the mean integrated fluorescence signal during each puff ($\Delta F/F_0$ * s; a measure of the cumulative amount of Ca^{2+} released during a puff) remained about constant (Fig. 2G). Thus, the marked decline in overall puff activity around the half-rise time of the global Ca^{2+} response reported by the SD signal (Fig. 2B) can be attributed primarily to a reduced frequency of puffs (Fig. 2D), rather than to a diminution in the mean amount of Ca^{2+} liberated by each puff.

The right-hand panels in Fig. 2H—N show corresponding records and measurements from the four cells showing 'fast' rising global Ca^{2+} responses. Plotted on a normalized timescale the changes in frequency and amplitude of puffs closely match those during slow rising responses. Fig. S4 further compares the distributions of the puff parameters (frequencies, amplitudes, durations, and integrals) during slow- and fast-rising global signals. Despite their occurrence on a more compressed timescale during the fast-rising responses, the overall magnitudes and kinetics of puffs were closely similar to those during slow responses.

3.4. Heterogeneity between puff sites

Inspection of puff traces revealed considerable heterogeneity between puff sites within each cell (e.g. fig. S3E and Fig. 3A). Some sites displayed only small events involving openings of only one or two IP_3R channels, whereas others showed much larger puffs. We thus segregated the pooled measurements of puff amplitudes from Fig. 2 into two populations; 'big' sites where at least one puff with an amplitude > 0.5 $\Delta F/F_0$ was observed (Fig. 3B; $n = 930$ events, 158 sites), and 'small' sites where no events > 0.5 $\Delta F/F_0$ were detected (Fig. 3C; $n = 367$ events, 133 sites). At big sites, large puffs occurred predominantly during the initial part of the response and progressively fewer large puffs were observed as the global signal rose, although numerous small events continued (Fig. 3B). Sites that showed only small puffs did not show any consistent decline in puff amplitudes (Fig. 3C). These behaviors are summarized in Fig. 3D, plotting mean puff amplitudes from big (filled red squares) and small (filled blue squares) sites, binned at normalized time intervals during the global response. The mean amplitude of events at big puff sites declined overall by about 50% over the time course of the puff flurry. This reduction could be attributed almost entirely to a fall-off in larger (> 0.5 $\Delta F/F_0$), events because the mean amplitude of small (< 0.5 $\Delta F/F_0$) puffs at the same sites remained about constant during the flurry (open red squares, Fig. 3D), closely matching the behavior of puffs at small puff sites (filled blue squares). In contrast to the difference in temporal evolution of puff amplitudes between big and small puff sites, the temporal evolution of overall event frequencies was similar at both types of sites (Fig. 3E,F).

3.5. Dwell-state amplitudes

The amplitude of a puff is a function of both the number of IP_3R channels that are open at the peak, and the fluorescence signal arising from Ca^{2+} flux through each open channel [22]. To better assess how the Ca^{2+} flux through individual IP_3R channels might change during the rise of global Ca^{2+}signals we measured the amplitudes of dwell-state levels (Fig. 4A) - steps during puffs that reflect differing numbers of IP_3R channels open at different times during a puff - and the amplitudes of small, 'square' events (blips) that result from opening of a single channel [20–22]. Figs. 4B,C show, respectively whole-cell Cal520 $\Delta F/F_0$ and SD traces obtained from imaging records in five cells, acquired at a faster frame rate than in Figs. 2 and 3 to better resolve individual fluorescence step-levels. Fig. 4D shows a scatter plot of all dwell-state amplitudes during the rise of the global responses. Although there was a marked decline in the size of the largest events, an underswell of a greater number of smaller events continued. The mean fluorescence dwell-state amplitude late in the puff flurry (from 20 to 25 s) was thus only modestly lower compared to the beginning (5–10 s): $\Delta F/F_0$ 0.254 ± 0.009 vs. 0.409 ± 0.027. The mean frequency of dwell-state events matched the time course of the global SD signal, rising to a maximum during the foot of the global Ca^{2+} response and declining abruptly at about the mid-point of the global Ca^{2+} rise (Fig. 4E).

Prompted by our analysis of peak puff amplitudes at big and small puff sites (Fig. 3), we further segregated measurements of dwell-state event amplitudes from big sites where at least one puff > 0.5 $\Delta F/F_0$ was observed (Fig. 4F; $n = 787$ events, 23 sites), and small sites where no events exceeded 0.5 $\Delta F/F_0$ (Fig. 4G; $n = 424$ events, 20 sites). At sites giving large puffs, high amplitude dwell-states were most apparent early during the puff flurry, whereas numerous small events continued with undiminished amplitude (Fig. 4F); as did dwell-state amplitudes at sites that showed only small puffs (Fig. 4G). These behaviors are summarized in Fig. 4H, plotting mean dwell-state levels binned at time intervals during the global response. The overall mean amplitudes of dwell-states at big puff sites declined to about one half over the time course of the puff flurry (Fig. 4H, filled red circles). Similar to the trends observed for peak puff amplitudes this decrease could be attributed almost entirely to a fall-off in larger (> 0.5 $\Delta F/F_0$) dwell-states, as the mean amplitudes of smaller (> 0.5 $\Delta F/F_0$) dwell-states at big sites remained steady (Fig. 4H, open red circles). The mean dwell-state amplitudes at sites generating only small puffs also remained almost constant (Fig. 4H, filled blue triangles). The frequencies of dwell-state events followed similar temporal patterns at both small and big sites (Fig. 4I,J).

3.6. Limits of resolution

To determine how our ability to detect and reliably measure puffs and blips might be impaired as photon shot noise increases during global Ca^{2+} responses we generated test data by synthesizing idealized local Ca^{2+} events of various amplitudes and added these throughout an experimental record of a global Ca^{2+} response in a cell pre-treated with

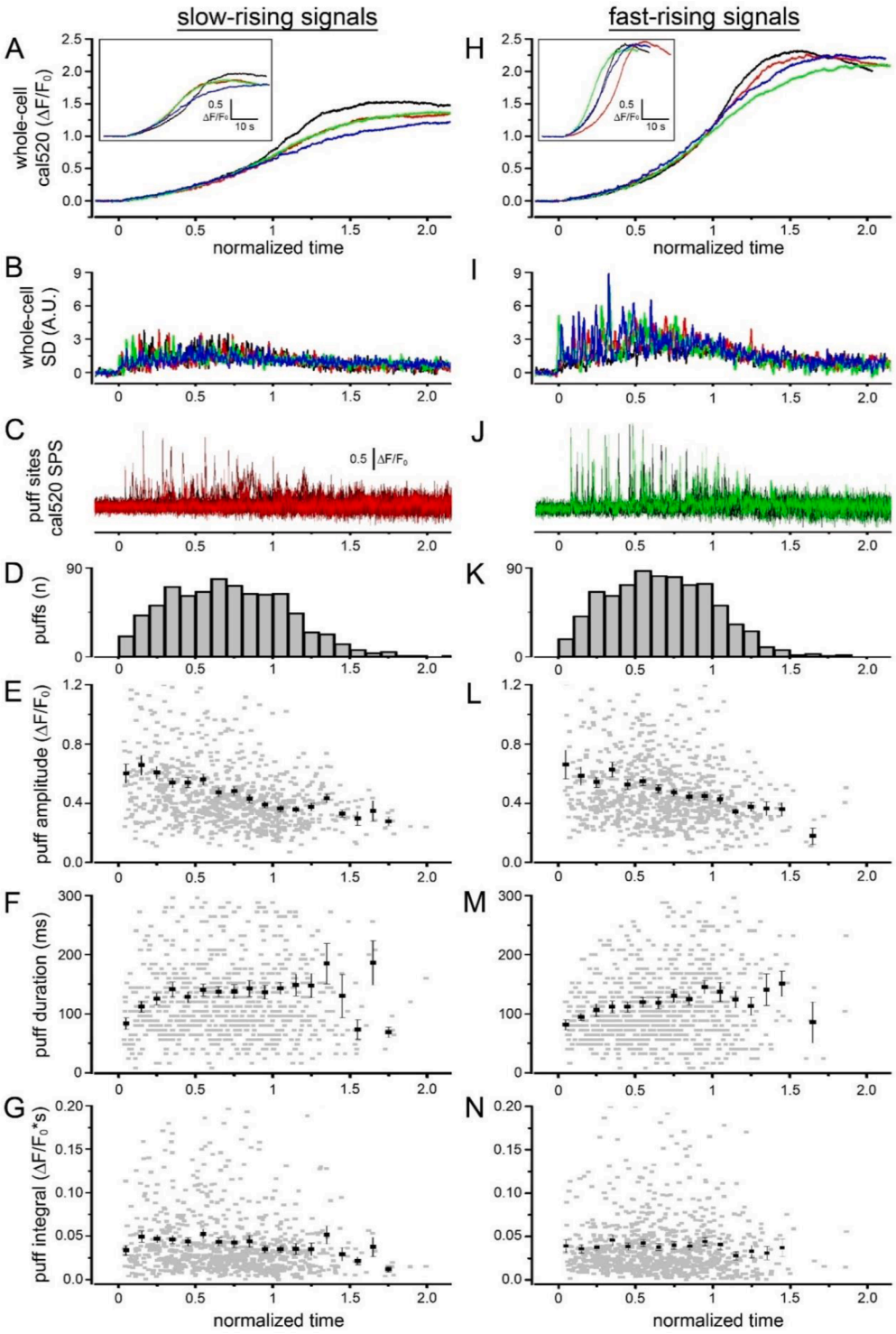

Fig. 2.. Frequencies, amplitudes, durations and integrals of puffs during slow- and fast-rising global Ca^{2+} responses. (A-G) Records are from 4 EGTA-loaded HEK cells that exhibited relatively slow-rising global Ca^{2+} signals in response to photoreleased i-IP_3. (A) Overlaid traces (each cell a different color) show whole-cell Cal520 $\Delta F/F_0$ signals. To compensate for minor differences in time course between the cells (*inset*), data in the main graph, and in other panels are depicted on a normalized timescale, with $t = 0$ corresponding to the time of the photolysis flash and $t = 1$ the time when the global Ca^{2+} signal rose to 50% of its peak in each cell. (B) Superimposed traces show corresponding whole-cell SD signals. (C) Overlaid traces of representative puff activity (Cal520 $\Delta F/F_0$ after SPS processing) at 12 sites in one cell. (D) Frequencies of Ca^{2+}puffs (total numbers of events from four cells per normalized 0.1 time interval) during the rise of the global signal. (E-G) Plots show measurements of individual puffs (gray) and mean values per binned time interval (black, ± 1 SEM) during the rise of the global signal. (E) Puff amplitudes, $\Delta F/F_0$, measured as rise from the immediately preceding baseline to peak. (F) Puff durations, measured as time the fluorescence remained above 20% of the peak value. (G) Puff integrals, measured as the area under each Ca^{2+} puff in units of $\Delta F/F_0$*s. (H—N) Corresponding data from 4 cells that exhibited faster-rising global Ca^{2+} signals. Data are from 788 puffs in (D-G) and 793 puffs in (K-N). For clarity of presentation the y-axes are scaled so that a few (< 5%) individual data points are truncated.

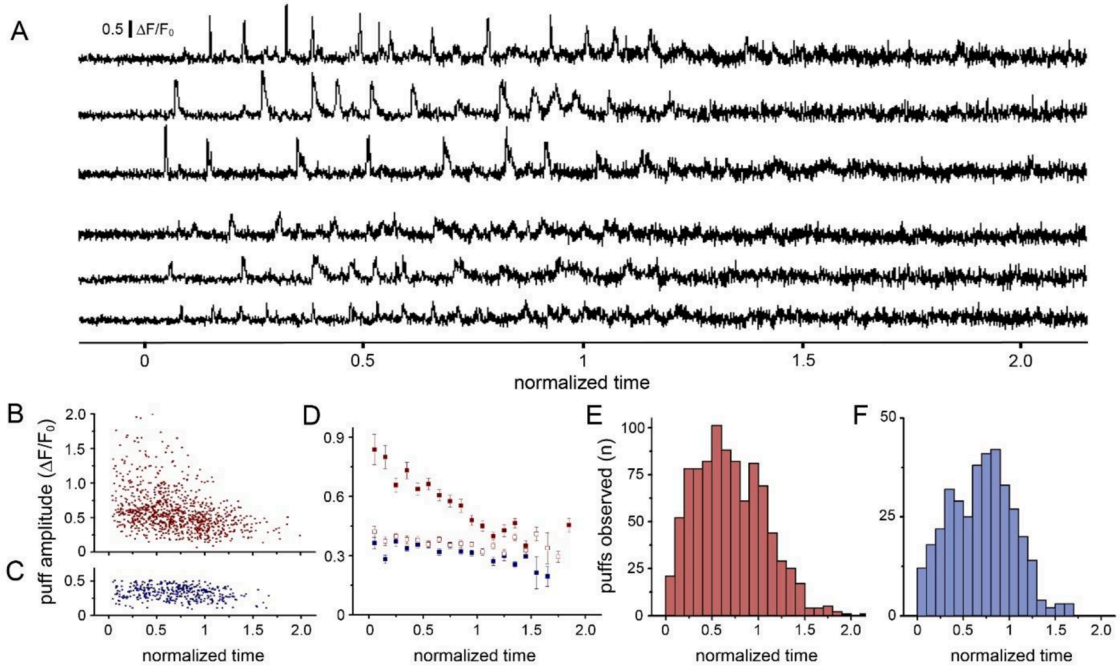

Fig. 3.. Differing evolution of puff amplitudes at sites showing large, or only small events. (A) Representative examples of i-IP_3-evoked Ca^{2+} puffs in EGTA-loaded HEK cells, shown on a normalized timescale as in Fig. 2. Traces show SPS-corrected Cal520 fluorescence $\Delta F/F_0$ from 3 × 3 pixel (1.5 × 1.5 μm) ROIs. The upper three traces are from sites that generated large puffs, and the lower three traces from sites where only small puffs occurred. (B) Plot of individual puff amplitudes as a function of normalized time from a subset of 158 'big' sites where at least one puff was observed with an amplitude > 0.5 $\Delta F/F_0$. (C) Scatter plot of puff amplitudes from 133 'small' puff sites where no puff was greater than 0.5 $\Delta F/F_0$. (D) Mean puff amplitudes at big and small puff sites, binned at normalized time intervals throughout the global response. Filled red squares are means of all puffs at big sites; open red squares are means of puffs at big sites excluding events > 0.5 $\Delta F/F_0$; blue squares are means of all puffs at small sites. Error bars are ± 1 SEM. (E,F) Frequencies of puffs (numbers of events per normalized time bin) throughout the global response plotted, respectively, for those sites exhibiting large or only small events. Data were derived from the cells illustrated in Fig. 2 and fig. S4.

cyclopiazonic acid (CPA) to inhibit puff activity [16] that was of similar amplitude to the records in Fig. 2A,H but was substantially free of any local fluctuations. The resulting image stacks were processed identically to the experimental puff data and, with the observer blinded as to the random timing of simulated events, were analyzed by automated puff detection in FLIKA (fig. S5A-E), by visual inspection (fig. S5F-J), and by using our SD routine (fig. S6A-D).

Fig. S5A shows the whole-cell Ca^{2+} fluorescence signal from the image stack to which 'square' (120 ms duration) channel-like events were added at random times with fluorescence amplitudes ($\Delta F/F_0$) of: 0.08, 0.12, 0.16, and 0.24 (fig. S5B-E, respectively). Although many of the smallest events tested (0.08 $\Delta F/F_0$) were below the algorithm's detection limit, simulated events approximating that evoked by a single IP_3R channel [20] (0.12 $\Delta F/F_0$) were detected by the algorithm with a 58% success rate and identified equally well at the beginning of the global response as at the peak. Simulated events of larger amplitudes ($\Delta F/F_0$ 0.16, and 0.24) were readily resolved (84% and 95% detected, respectively). In all cases FLIKA typically overestimated the true simulated event amplitude (fig. S5B-E, dashed lines). This was expected as the algorithm was designed to detect peaks and would be biased by baseline noise spikes superimposed on the synthetic Ca^{2+} signals. Visual inspection of the same simulations detected events with similar fidelity to FLIKA, but more closely matched the simulated event amplitudes (fig. S5G-J) because, as with the data in Fig. 4, we interpolated mean amplitude measurements within noise fluctuations during the events.

Because these simulations indicated that a proportion of small ($\Delta F/F_0 < 0.2$) Ca^{2+} events might have been missed as global Ca^{2+} signals approached their peak we further tested the ability of the SD routine to report the activity of such small events. Using a similar base image stack (fig. S6A), we added randomly occurring events of two different amplitudes at 25 sites, beginning at the onset of the global response. Maximum-projection SD images clearly revealed simulated local events with amplitudes of $\Delta F/F_0$ 0.125 (fig. S6C) and 0.25 (fig. S6D) during both the initial rise of the global signal and the subsequent rise to peak that were absent from simulations with no add events (fig. S6B). Moreover, corresponding traces of the SD signal measured from the whole cell showed a sustained elevation when simulated events were present throughout the global Ca^{2+} rise (fig. S6C,D), without the marked decline at the mid-point of the Ca^{2+} rise characteristic of IP_3-evoked responses like those in Fig. 2.

We thus conclude that the marked decline in puff activity around the time of half-rise of the global signal that we report does not arise artifactually from a failure to resolve putative events, or from an underestimate of event amplitudes.

3.7. *Single-channel Ca^{2+} flux when ER Ca^{2+} content is replete or partially depleted*

In light of our finding that the rundown in puff activity during global responses is associated with declining levels of Ca^{2+} in the ER [16], we considered whether the decrease in puff amplitudes (Fig. 3D) might simply result from an attenuated driving force for Ca^{2+} efflux through IP_3R channels. We thus compared fluorescence signals arising from single channel openings (blips) under conditions when the ER Ca^{2+} levels were expected to be replete, or partially depleted. Prior treatment with the SERCA inhibitor CPA to partially deplete ER Ca^{2+} content activity substantially abolishes puff activity while preserving diffuse global Ca^{2+} responses [16]. In some cells treated with CPA we still observed weak punctate activity, evident as hot spots of local Ca^{2+} release in maximum intensity projections of SD image stacks (Fig. 5A) and as small whole-cell SD signals during the initial rise of the global responses (Fig. 5B). Fluorescence traces from hotspots showed discrete Ca^{2+} transients, most with amplitudes and 'square' time course (Fig. 5C) characteristic of single-channel IP_3R openings [21,22]. These events

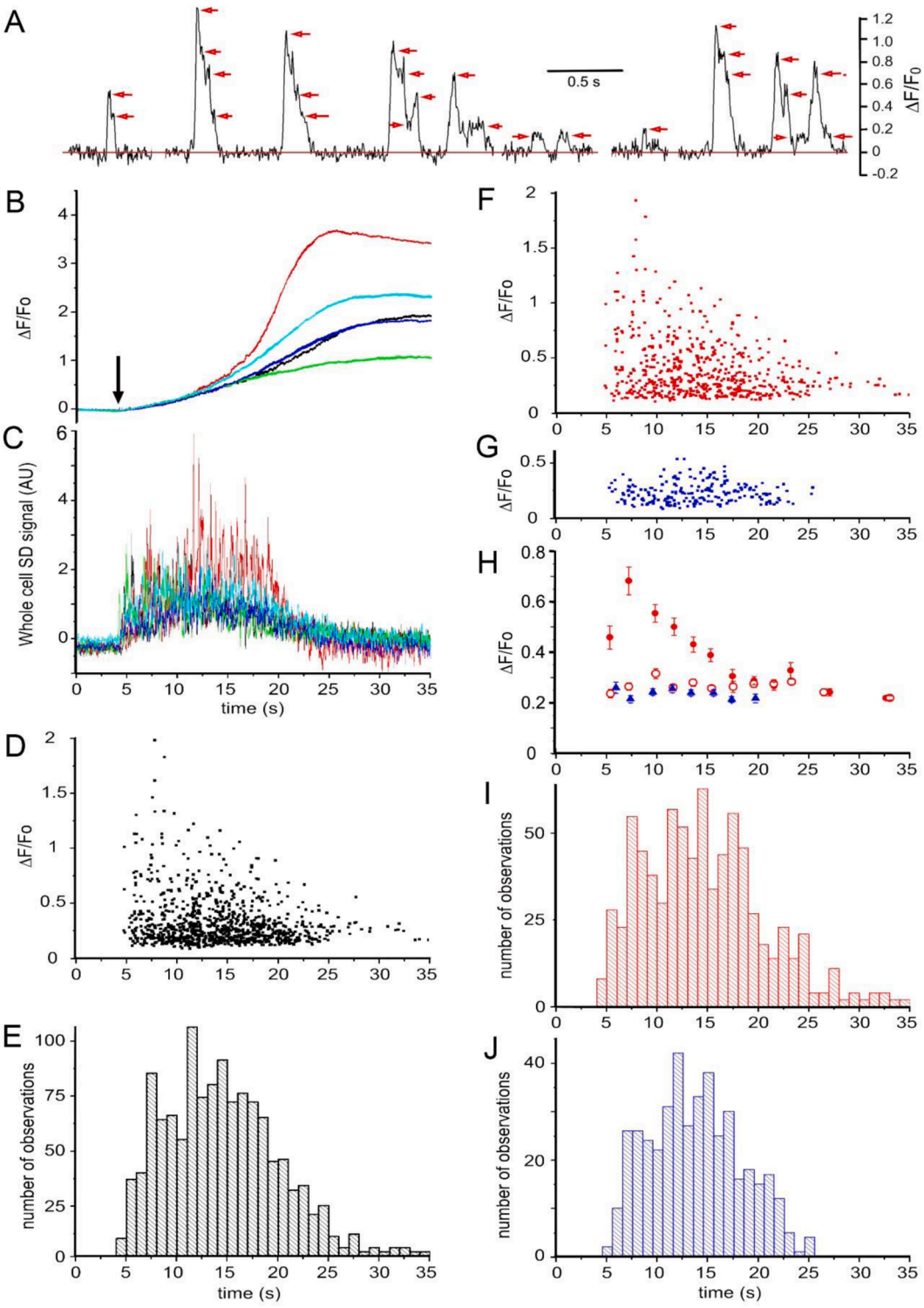

Fig. 4.. Dwell-state amplitude measurements. (A) Examples of puffs and single-channel events illustrating different dwell-state levels (red arrows) of Cal520 Ca^{2+} fluorescence signal during individual puffs. (B) Superimposed traces show global Ca^{2+} signals ($\Delta F/F_0$) evoked in 5 HEK cells by photorelease of i-IP_3 when marked by the arrow. (C) Corresponding whole-cell SD signals. (D) Pooled data plotting all dwell-state amplitudes measured from 43 puff sites. (E) Frequency of occurrence of all dwell-state events binned at 2 s intervals throughout the global Ca^{2+} responses. (F) Pooled data plotting dwell-state levels measured from a subset of 23 sites where at least one puff was observed with an amplitude > 0.5 $\Delta F/F_0$. (G) Pooled data plotting dwell-state amplitudes measured from a subset of 20 puff sites where no events greater than 0.5 $\Delta F/F_0$ were observed. (H) Mean dwell-state amplitudes at those sites exhibiting large events (filled red circles) and amplitudes at these big sites excluding events > 0.5 $\Delta F/F_0$ (open red circles); and mean dwell state amplitudes at those sites exhibiting only small events (blue triangles). Error bars are $\pm$ 1 SEM. (I,J) Frequencies of occurrence of dwell-state events plotted, respectively, for sites exhibiting large or only small events.

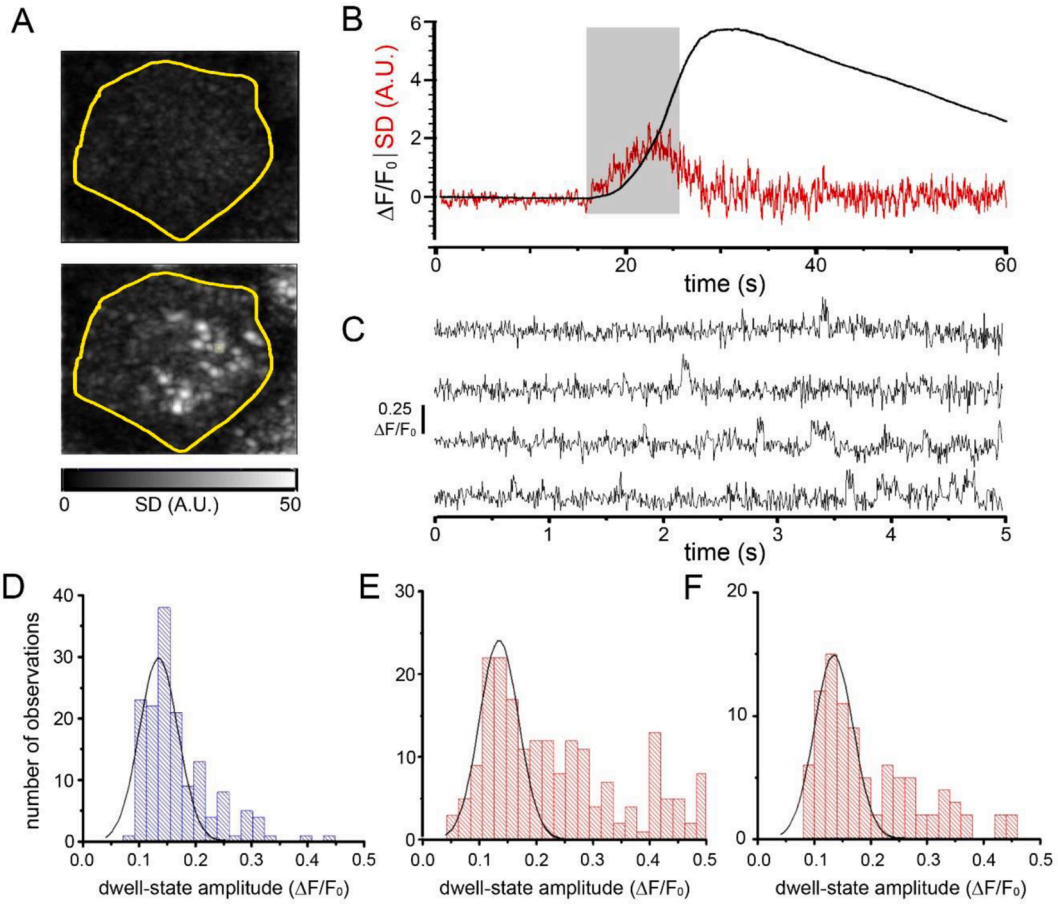

Fig. 5.. Amplitudes of single-channel Ca^{2+} signals when the ER Ca^{2+} content is replete or partially depleted. (A-C) Representative data are from a HEK cell not loaded with EGTA that was exposed to CPA (50 μM) for 1 min and then maintained in Ca^{2+}-free medium for 30 min before imaging. Photorelease of i-IP_3 evoked a substantial global rise in Ca^{2+} and, although puff activity was strongly suppressed, some small, local Ca^{2+} transients were still evident. (A) Maximum intensity projections (1250 frame, 10 s) from the SD image stack before the photolysis flash (top), and during the rising phase of the global signal (bottom). (B) Traces show the global $\Delta F/F_0$ signal (black) and SD signal (red) derived from a ROI encompassing the whole cell. Gray box indicates the time period used to generate the lower panel in A. (C) Traces show Ca^{2+} activity ($\Delta F/F_0$) at four of the hotspots identified in the lower panel of A, displayed on an expanded timescale beginning at the onset of the SD signal. (D-F) Plots show distribution histograms of dwell-state amplitudes recorded in different situations. The black curves are Gaussian distributions with the same mean (0.135 $\Delta F/F_0$) and standard deviation (0.069 $\Delta F/F_0$) but scaled individually in amplitude to match the data in each panel. (D) Distribution of step-level amplitudes in three cells that had been pre-treated with CPA to partially deplete the ER Ca^{2+} store content. The Gaussian fit was determined from these data. (E) Distribution of step-level amplitudes from naïve EGTA-loaded cells (the same data set as in Fig. 4E) measured during the initial 8 s following photorelease of i-IP_3. (F) Distribution of step-level amplitudes from the same sites as in E at times between 16 and 32 s following photorelease of i-IP_3 when the event frequency had markedly declined.

provided an opportunity to examine whether Ca^{2+} flux through single IP_3R channels was diminished when punctate activity was substantially suppressed by prior reduction of the ER Ca^{2+} content.

Fig. 5D shows the distribution of event amplitudes in three CPA-treated cells. The measurements largely cluster around a single peak and fit well to a Gaussian distribution with a mean of 0.135 $\Delta F/F_0$. We interpret this value as a measure of single-channel Ca^{2+} flux in light of the 'square' appearance of these events and the similarity of their magnitudes to prior Cal520 measurements of single IP_3R channel signals in WT HEK cells (0.126 $\Delta F/F_0$) [20], as well as those obtained with a less sensitive indicator (0.11 $\Delta F/F_0$) [21,22].

To compare this estimate of single-channel Ca^{2+} flux to that when the ER Ca^{2+} content is replete or declining during IP_3-evoked global responses, we further plot in Fig. 5E,F dwell-state amplitude distributions from the cells in Fig. 4. The data in Fig. 5E were obtained during the first 8 s of the puff flurry, before the ER Ca^{2+} content would have been appreciably depleted, whereas the data in Fig. 5F were obtained during the last 16–32 s when puff activity had markedly declined. The initial peaks of these two distributions match closely with one another, and with the distribution of events in CPA-treated cells (Fig. 5D); as illustrated by the superimposed black curves which replicate the Gaussian distribution fitted to the distribution of event amplitudes in CPA-treated cells after scaling in the y-axis to match the differing numbers of observations.

A possible caveat in this comparison is that the CPA-treated cells were not loaded with EGTA. However, because buffering by EGTA is too slow to appreciably affect the amplitudes of the fast, local Ca^{2+} fluorescence transients [29] (fig. S1), we conclude that the similar fluorescence amplitudes in Fig. 5D-F indicate that single-channel Ca^{2+}flux is not appreciably diminished when the ER Ca^{2+}content is reduced by prior SERCA inhibition, or by release of Ca^{2+}during global IP_3-mediated responses.

3.8. *Cumulative Ca^{2+} liberation by puffs*

In EGTA-loaded cells the local fluorescence signal recorded by TIRF microscopy at puff sites closely tracks the instantaneous Ca^{2+} flux through open IP_3R channels [33,34]. Thus, the integral under local fluorescence traces of puffs provides a relative measure of the cumulative amount of Ca^{2+} liberated by punctate release during a puff flurry.

We utilized two approaches to calculate integrals; by directly estimating the area under local fluorescence traces from puff sites (Fig. 6A-E), and by using automated FLIKA analysis to sum the integrals under successive individual puffs (Fig. 6F-J).

A crucial requirement for the first approach is that the baseline is stable around zero, because any systematic deviations would accumulate large errors over time. After stripping off the global Ca^{2+} elevation using our SPS algorithm we then corrected any remaining baseline deviations (typically $\Delta F/F_0 < 0.2$) by manually fitting a 20-point spline function using the baseline tool in Microcal Origin. Figs. 6A,B illustrate representative fluorescence ratio ($\Delta F/F_0$) traces from three puff sites after baseline correction, together with their respective cumulative integrals. As expected, the cumulative integrals show stepwise increases associated with each puff, and plateau when puff activity stops. The $\Delta F/F_0$ trace in Fig. 6C shows the sum of puff activity at 11 sites in a single cell, and the red trace in Fig. 6D plots the cumulative integral under that trace, alongside the global fluorescence signal from the entire cell (black trace, normalized to facilitate comparison). Similar data from five cells (different colors) are shown superimposed in Fig. 6E, with noisier traces on the left showing the sum of cumulative integrals from multiple sites in each cell and smoother traces on the right showing the corresponding increases in global Ca^{2+} signal in that cell. To facilitate comparison between punctate Ca^{2+} release and the global Ca^{2+} signal the amplitudes of all traces are scaled to the same peak height and are further normalized in time by aligning to the occurrence of the first puff (time zero) and stretching to align the time of half-maximal rise of the global signal (normalized time $t = 1$).

Figs. 6F-J show corresponding data obtained by our second approach, calculating the integrals under each detected puff using an automated algorithm in FLIKA. Fig. 6F illustrates data from three puff sites in the same cell, with the height of the bars representing the integral of each successive puff. The cumulative sum of these integrals (Fig. 6G) follows a pattern closely similar to that derived by integrating under fluorescence traces (Fig. 6B), as do mean cumulative integrals derived from all detected puff in a cell (Fig. 6H,I) and from multiple cells (Fig. 6J).

Both methods of analysis show that the cumulative release of Ca^{2+} via punctate activity precedes the global rise of Ca^{2+}, being substantially complete (~85%) at the time the global signal is half-maximal (Figs. 6E, J), thereby reaffirming our proposal that the subsequent rise of global Ca^{2+} is primarily driven by release from a source other than puff activity [16].

3.9. The SD signal faithfully reports Ca^{2+} flux during puffs

Although determination of cumulative integrals under puff traces provides a direct measure of punctate Ca^{2+} release, this is a technically exacting procedure. We were thus interested to determine how well these measurements compared with more facile measurements of local and global SD signals.

Fig. S7A shows a scatter plot of measurements from 52 individual puffs, plotting the amplitude of the SD signal (y-axis) vs. the peak

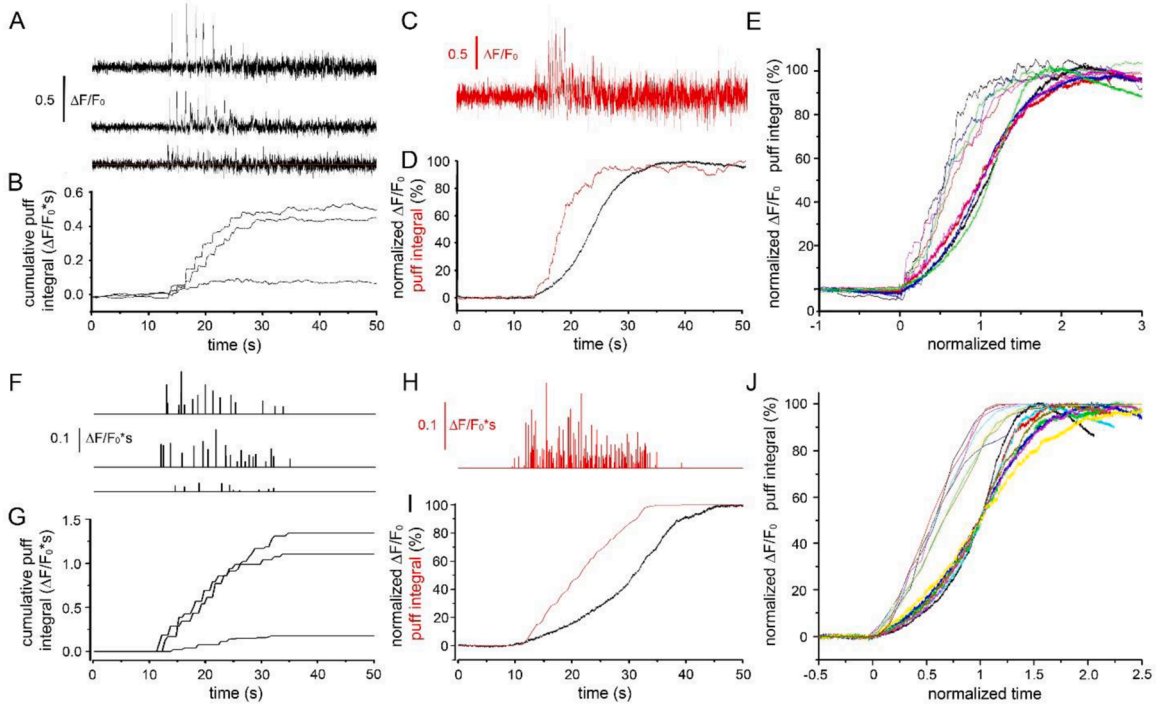

Fig. 6.. Estimating cumulative Ca^{2+} liberation via punctate release by integrating under puff traces. Estimates of the cumulative amount of Ca^{2+} released by puffs during global responses were made by integrating under fluorescence traces from selected puff sites (A-E) and by summing the integrals under individual puffs as derived by FLIKA analysis (F-J). (A) Traces show representative puffs evoked by photorelease of i-IP_3 at three sites in the same cell. The $\Delta F/F_0$ signal was flattened by first applying the SPS algorithm and then correcting residual baseline fluctuations by manually fitting a 20-point spline function using the 'baseline' function in Microcal Origin. (B) Respective cumulative integrals under the three traces in A. (C) Summation of $\Delta F/F_0$ records from 11 sites in a different cell. (D) Red trace shows the cumulative integral under the trace in C. Black trace shows the global rise in $\Delta F/F_0$ signal from the whole cell. To facilitate comparison, both traces are scaled to the same peak amplitude (100%). (E) Superimposed scaled traces plotted on a normalized time scale from five cells (different colors) showing cumulative integrals of puff activity (noisier traces to the left) and global $\Delta F/F_0$ signals (right). (F-J) Corresponding data derived from different cells using automated measurement by FLIKA to calculate integrals under individual puffs. (F) Bars indicate the integrals of Ca^{2+} puffs at three different sites in the same cell during a global cytosolic Ca^{2+}response. (G) Respective cumulative sum of the traces in F. (H) Summation of puff integral trace measurements from all detected Ca^{2+} puffs within a single cell. (I) Red trace shows the cumulative sum of the integral trace in H, and the black trace shows the global Ca^{2+} signal, both scaled to a peak amplitude of 100%. (J) Superimposed traces plotted on a normalized time scale from eight cells (different colors) showing cumulative integrals of puff activity (traces to the left) and global $\Delta F/F_0$ signals (to the right).

amplitude of the local $\Delta F/F_0$ signal (x-axis) for the each event. The data fit well to a linear relationship, indicating that the SD signal, on average, provides a good measure of peak puff amplitude, although there is appreciable scatter among paired measurements of individual puffs. Fig. S7B compares paired measurements of cumulative punctate Ca^{2+} release obtained by integrating the areas under the whole-cell SD trace and under the $\Delta F/F_0$ trace, summed from multiple sites as in Fig. 6D. The time course of Ca^{2+} liberation derived by these two approaches correspond closely, although with a consistent tendency for the puff integral to approach a plateau more rapidly than the SD integral. This relationship is further illustrated in fig. S7C showing a scatter plot of measurements in five cells of SD integral vs. puff integral. The data closely approximate a linear relationship, but with a small deviation at higher values arising because the cumulative puff integral approaches a plateau value more rapidly.

3.10. Amount of Ca^{2+} liberated during a puff flurry

Measurements of the areas under Ca^{2+} fluorescence signals during a puff flurry allow us to estimate in absolute terms (moles) the cumulative amount of Ca^{2+} liberated into the cytosol by punctate release. Under our present recording conditions, we estimate that the Ca^{2+} flux through a single open IP_3R channel generates a mean local fluorescence signal of 0.135 $\Delta F/F_0$ (Fig. 5D-F, and see [20–22]). Further, the Ca^{2+} current passing through a single IP_3R under physiological conditions has been estimated to be about 0.15pA [35], corresponding to a Ca^{2+} flux of 7.5×10^{-19} mol s^{-1}. Thus, if a single channel were to remain open for 1 s, the integral under the fluorescence trace (0.135 $\Delta F/F_0$ * s) would be equivalent to a cumulative liberation of 7.5×10^{-19} mol of Ca^{2+} into the cytosol.

Taking as an example the top trace in Fig. 6F,G, the cumulative integral under the puffs at this individual site was about 1.4 $\Delta F/F_0$ * s, corresponding to the liberation of about 7.8×10^{-18} mol of Ca^{2+}. The sum of integrals from all sites detected by the FLIKA algorithm in the cell (Fig. 6H,I) was 6.56 $\Delta F/F_0$ * s, equivalent to liberation of 3.6×10^{-17} mol Ca^{2+}. From similar measurements in eight cells we obtained a mean value for punctate Ca^{2+} liberation of $4.38 \pm 0.42 \times 10^{-17}$ mol (43.8 attomoles). This number reflects activity only at those puff sites detected within the TIRF footprint of the cell. Assuming a similar density of sites across the surface of the cell [36], and that the footprint of these highly flattened cells represents about one half of the total membrane area, we therefore estimate the total punctate release of Ca^{2+} into the cytosol to be roughly 90 attomoles.

We can further estimate the minimum number of functional IP_3R channels that must be present within the TIRF field by using the peak amplitude of the largest puff observed at each site as an indication of the number of channels simultaneously open at that site. Taking the cell in Fig. 6F-I as an example, the sum of amplitudes of the greatest puff observed at each of 97 sites was 40 $\Delta F/F_0$, giving an estimate for the total number of channels of 296 (again, assuming a single-channel signal of 0.135 $\Delta F/F_0$). The puff flurry during which these channels were active lasted about 22 s (Fig. 6I) and, as calculated above, resulted in a cumulative Ca^{2+} liberation of 3.6×10^{-17} mol. This would correspond to a mean of 2.2 channels remaining continuously open throughout the 22 s flurry, giving an estimated mean open probability among the 296 channels of $P_{open} = 0.007$. From the 8 cells in Fig. 6J the mean $P_{open} = 0.0088 \pm 0.001$ during puff flurries with durations ranging between 13 and 47 s.

3.11. Kinetics and relative magnitudes of punctate and diffuse modes of Ca^{2+} liberation

Having established that integration of fluorescence signals at puff sites provides a measure of punctate Ca^{2+} release, we could then address the relative contributions of punctate versus diffuse modes of Ca^{2+}release during global Ca^{2+} responses. Figs. 7A,B illustrate our procedure, using data from a representative cell. We first derived the kinetics of Ca^{2+} flux into the cytosol through IP_3Rs on the basis that the change in global fluorescence signal at any given time reflects a balance between rates of Ca^{2+} release into and out of the cytosol. To obtain a rate constant for removal of cytosolic Ca^{2+} we fitted a single exponential to the decaying fluorescence signal of Cal520 following transient photorelease of Ca^{2+} from a caged precursor loaded into the cytosol of HEK cells [16]. As illustrated in Fig. 7A, we then differentiated the whole-cell fluorescence Ca^{2+} signal (black trace) and added to this the estimated rate of Ca^{2+} removal at each time point to derive the time course of total Ca^{2+} flux into the cytosol (cyan trace). By comparison, the blue trace shows puff integrals, reflecting punctate Ca^{2+} flux into the cytosol.

To estimate the proportion of the total IP_3-evoked Ca^{2+} flux contributed by punctate release we made a simplifying assumption that the initial, abrupt increase in total flux arose almost entirely from puffs, on the basis that puff activity is high during the first few seconds of the response when the global fluorescence signal shows only a small initial rise. In Fig. 7B we thus superimpose on the total Ca^{2+} flux trace (cyan) a smoothed trace of the puff integrals (blue) after scaling the latter to overlay the initial few seconds of the total Ca^{2+} flux increase. The

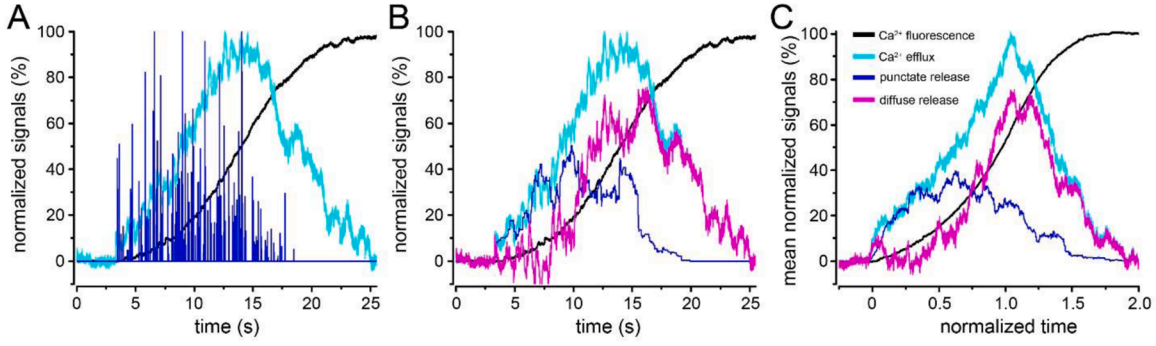

Fig. 7.. Kinetics and relative contributions of punctate and diffuse modes of Ca^{2+} release during IP_3-mediated global Ca^{2+} signals. (A) Representative records from a single EGTA-loaded HEK cell. Traces (scaled to the same peak height) show the whole-cell Cal520 fluorescence $\Delta F/F_0$ (black), summed puff integral measurements from all detected Ca^{2+} puffs at the times of their occurrence (blue), and the estimated rate of Ca^{2+} efflux into the cytosol (cyan). The rate of Ca^{2+} efflux was derived by differentiating the Cal520 $\Delta F/F_0$ trace and adding to it an estimated rate (0.2 s^{-1}) of Ca^{2+} removal from the cytosol. (B) Traces showing Ca^{2+} fluorescence (black) and estimated Ca^{2+} efflux (cyan) are replicated from A. The blue trace depicts the summated puff integral trace from A, after strong smoothing (200 point, 1.6 s, adjacent averaging) and scaling in amplitude to match the initial portion of the Ca^{2+} efflux trace. The magenta trace shows the difference between the cyan (total Ca^{2+} efflux) and blue (punctate release) traces, giving an estimate of the magnitude and time course of Ca^{2+} liberation by diffuse mode Ca^{2+} release. (C) Mean traces from seven cells showing normalized global Ca^{2+} fluorescence(black), estimated total Ca^{2+} efflux (cyan), punctate release (blue), and diffuse release (magenta).

difference between these traces (magenta trace) represents the additional Ca^{2+} flux that we attribute to diffuse mode release. Fig. 7C shows mean data derived in this way from seven cells, plotted on a normalized timescale. The integrals under the traces provide a proportional measure of the cumulative amounts of Ca^{2+} liberated by punctate and diffuse release modes during the rise to the peak of the IP_3-mediated global response. From Fig. 7C we estimate that punctate Ca^{2+} release contributes 39.7 ± 3.3% of the total, and diffuse release the remaining 60.3%.

4. Discussion

4.1. Punctate and diffuse modes of IP_3-mediated Ca^{2+} liberation

We had previously shown that global IP_3-mediated Ca^{2+} signals involve two modes of Ca^{2+} liberation: 'punctate' release as a flurry of transient, local puffs during the initial rise of global Ca^{2+}, with the subsequent rise sustained by a distinct 'diffuse' release mode[16]. In those experiments we monitored puff activity via a statistical, population measure of Ca^{2+} fluctuations (SD signal), and now describe recordings of individual puffs that provide further insight into the mechanisms that terminate the flurry of puff activity.

In Fig. 2 we show that the decline in puff activity and its near cessation midway during the rise of a global Ca^{2+} signal are associated with both a decrease in amplitude of individual puffs and a marked fall-off in their frequency. The former effect, however, is minor. The decline in amplitude was restricted to a few sites in each cell that generated large amplitude puffs, where the largest puffs appeared early during the flurry and then progressively diminished in amplitude. However, an underswell of small events continued with undiminished amplitudes, so that the mean puff amplitude at these 'big' puff sites declined <50% from beginning to end of the puff flurry. At other, more numerous sites that showed only small puffs, their mean amplitude did not decline appreciably throughout the flurry. Averaged across all sites the mean amplitude of puffs declined by only about 35% during the flurry. Moreover, this modest decrease in puff amplitudes was counterbalanced by an increase in mean puff duration, such that the average amount of Ca^{2+} liberated per puff remained substantially constant throughout the flurry.

In contrast, the mean frequencies of puffs averaged across sites throughout the TIRF footprint showed a progressive rise and then abrupt fall, following a time course that closely matched the punctate activity reported by the whole cell SD signal. A large majority (75%) of puffs arose before the global Ca^{2+} signal reached half-maximal and, correspondingly, cumulative liberation of Ca^{2+} liberation through puffs was >80% complete by this time.

4.2. Amounts of Ca^{2+} liberated by punctate and diffuse release

We estimate the amount of Ca^{2+} liberated by puffs into the cytosol of a cell during a typical i-IP_3-evoked global Ca^{2+} signal to be about 90 atttomoles (9×10^{-17} mol). This value derived from summing the durations for which individual IP_3R channels were open. It is thus independent of any assumptions of indicator affinity or presence of cytosolic Ca^{2+} buffering, but does depend on other assumptions, notably estimates of the physiological Ca^{2+} flux through a single type 3 IP_3R channel obtained in a different cell type [35]. The volume of a HEK cell is about 3000 μm^3 (3×10^{-12} liters or 3 femtolitres). Assuming that the cytosol and nucleosol make up one half of that volume, diffusion of the Ca^{2+}liberated by puffs would result in a Ca^{2+} concentration rise of 60 μM. Under physiological conditions we further estimate that puffs contribute only about 40% of the total IP_3-mediated Ca^{2+} liberation, giving a total Ca^{2+} concentration rise of roughly 150 μM. The peak free Ca^{2+} concentration rise for IP_3-evoked global responses in naïve HEK cells is reported to be less than 1 μM [37], suggesting a minimal endogenous Ca^{2+} buffering power of about 150; compatible with the wide range (tens to >100) reported for various other cell types [38].

4.3. Termination of puff activity

What might underlie the declines in puff amplitudes and frequencies during the rising phase of global Ca^{2+} responses? They cannot be attributed to a decay of i-IP_3 concentration, because photoreleased i-IP_3 is slowly degraded, and at low levels of i-IP_3 that evoke little rise in global Ca^{2+} puffs persist for minutes with stable amplitudes and frequency [29,39]. Based on our earlier findings that puff activity is reduced or abrogated by partial depletion of the ER Ca^{2+} content, but not by prior elevation of cytosolic free [Ca^{2+}] [16], we propose that a declining concentration of Ca^{2+} in the ER lumen is the controlling factor. This then raises further questions. How may the luminal Ca^{2+} level affect the net flux through IP_3Rs at puff sites? Is the fall in luminal Ca^{2+} driven by puff activity or diffuse release?

A simple explanation for the overall decline in puff amplitudes during the rise of global Ca^{2+}could be that Ca^{2+}flux through each open IP_3R channel diminishes as a result of the reduced electrochemical driving force as Ca^{2+} levels fall in the ER lumen. Several observations, however, argue that this is not a major factor. The decrease in amplitude was restricted to large puffs that involve concerted opening of several IP_3Rs, while the mean amplitudes of small puffs at the same sites, as well as puffs at other sites that evoked only small puffs, remained steady. Similarly, measurements of the unitary Ca^{2+} signals (blips) generated by Ca^{2+} flux through openings of individual IP_3R channels [21,22], did not show any measurable change throughout the puff flurry. Moreover, although pre-treatment with CPA to partially deplete the ER Ca^{2+} content strongly attenuated puff activity evoked by photoreleased i-IP_3, the mean amplitude of remaining blips was comparable to that in control cells. We thus conclude that the reduced overall amplitude of puffs - driven by the marked attenuation of 'large' puffs - does not arise in direct proportion to a reduced driving force for Ca^{2+}, which is expected to vary as a linear function of ER [Ca^{2+}] [40]. Nevertheless, it is possible that a fractional decrease in single-channel Ca^{2+} flux that was too small for us to resolve might account for the decline of large puffs. Because puffs involve regenerative opening of channels via CICR [5,11,23,24] a small reduction in Ca^{2+} flux might result in an exaggerated, non-linear reduction in puff amplitude. A reduced single-channel Ca^{2+} flux would not, however, explain the fall off in frequency of either puffs or blips, as the probability of channel opening is a function of the cytosolic concentrations of Ca^{2+} and IP_3 [7,8].

Our simulations with synthetic blip data indicate that the near cessation of punctate Ca^{2+}release does not arise artifactually because of a detection failure as noise levels rise along with the increasing fluorescence of the Ca^{2+} signal; nor did we see any indication that puffs progressively decline during the flurry to a point where they would become undetectable. Our observations thus point to a mechanism by which the decline of puff activity during global responses is mediated primarily through modulation of the gating of IP_3Rs, rather than a diminution in the Ca^{2+} flux through open channels. In light of findings that puff activity is abrogated by lowered levels of Ca^{2+}in the ER lumen [16], and conversely that the frequency of puffs is accelerated by elevated ER Ca^{2+} levels [41], we infer that luminal [Ca^{2+}] is the modulatory factor.

The issue of whether IP_3R channel activity is modulated, directly or indirectly, by [Ca^{2+}] in the ER lumen is controversial [35,42,43]. Patch-clamp recordings of IP_3Rs in isolated patches of nuclear membrane showed evidence only for feed-through modulation by Ca^{2+} flux through an open channel acting on functional binding sites on the cytosolic face of the channel, without evidence for intrinsic functional Ca^{2+}-modulatory sites on the luminal side of the channel [44]. However, putative accessory proteins would have been lost in the excised patch configuration, and nuclear IP_3Rs might not fully replicate the properties of the small numbers of 'licensed' IP_3Rs that generate puffs [15,20]. Regardless of specific mechanism, our observation of differential

run-down of big and small puffs at the same 'big' puff sites suggests that regulation does not act the level of IP_3R clusters, but rather at the level of individual IP_3R channels within a cluster.

Recent studies identify two different, putative mechanisms of luminal Ca^{2+} regulation of IP_3Rs via interacting Ca^{2+}-sensitive proteins. Vais et al. [45] describe regulation of IP_3R gating mediated by a Ca^{2+}-binding luminal protein – likely annexin A1 (ANXA1); and Emrich et al. [46] report that the STIM proteins that sense ER luminal Ca^{2+} levels to regulate plasmalemmal Orai channels [47] also modulate IP_3Rs by an unknown mechanism independent of Orai activation. Notably, both mechanisms operate such that IP_3Rs are inhibited under resting conditions when the ER Ca^{2+} is replete. The presence of ANXA1 on the luminal side of excised nuclear membranes was without effect on IP_3R gating when the luminal [Ca^{2+}] was low, but the open probability of the IP_3R channel dropped abruptly as luminal [Ca^{2+}] was raised above about 50μM [45]. Similarly, Emrich et al. [46] propose that unactivated STIMs inhibit IP_3R channels, and cells in which STIM1 and STIM2 were knocked out showed greater numbers of puffs and puff sites in response to photoreleased i-IP_3. It is thus difficult to reconcile either of these proposals with our findings that puff activity becomes depressed as ER Ca^{2+} levels fall during global signals. The mechanism underlying puff termination thus remains to be elucidated. On the other hand, relief from constitutive inhibition of IP_3Rs by ANXA1 or STIM as ER Ca^{2+} levels decline might contribute to a regenerative activation of the diffuse mode of Ca^{2+} liberation.

Funding sources

This work was supported by National Institutes of Health grant R37 GM048071 (IP).

Declaration of Competing Interest

All authors declare they have no competing financial interests.

Acknowledgements

We thank Dr. George D. Dickinson for creating the scaled peak subtraction (SPS) and puff simulator plugins for FLIKA used in this manuscript.

Supplementary materials

Supplementary material associated with this article can be found, in the online version, at doi:10.1016/j.ceca.2021.102494.

References

[1] M.J. Berridge, P. Lipp, M.D. Bootman, The versatility and universality of calcium signalling, Nat. Rev. Mol. Cell Biol. 1 (2000) 11–21, https://doi.org/10.1038/35036035.
[2] D.E. Clapham, Calcium Signaling, Cell 131 (2007) 1047–1058, https://doi.org/10.1016/j.cell.2007.11.028.
[3] Y. Yao, J. Choi, I. Parker, Quantal puffs of intracellular Ca2+ evoked by inositol trisphosphate in Xenopus oocytes, J. Physiol. 482 (1995) 533–553, https://doi.org/10.1113/jphysiol.1995.sp020538.
[4] I. Parker, Y. Yao, Regenerative release of calcium from functionally discrete subcellular stores by inositol trisphosphate, Proc. R. Soc. B Biol. Sci. 246 (1991) 269–274, https://doi.org/10.1098/rspb.1991.0154.
[5] I. Parker, J. Choi, Y. Yao, Elementary events of InsP3-induced Ca2+ liberation in Xenopus oocytes: hot spots, puffs and blips, Cell Calcium 20 (1996) 105–121, https://doi.org/10.1016/S0143-4160(96)90100-1.
[6] N.M. Woods, K.S.R. Cuthbertson, P.H. Cobbold, Repetitive transient rises in cytoplasmic free calcium in hormone-stimulated hepatocytes, Nature 319 (1986) 600–602, https://doi.org/10.1038/319600a0.
[7] M. Iino, Biphasic Ca2+ dependence of inositol 1,4,5-trisphosphate-induced Ca release in smooth muscle cells of the guinea pig taenia caeci, J. Gen. Physiol. 95 (1990) 1103–1122, https://doi.org/10.1085/jgp.95.6.1103.
[8] Ilya Bezprozvanny, J. Watras, B.E. Ehrlich, Bell-shaped calcium-response curves of Ins(l,4,5)P3- and calcium-gated channels from endoplasmic reticulum of cerebellum, Nature 351 (1991) 751–754.
[9] N.B. Thillaiappan, A.P. Chavda, S.C. Tovey, D.L. Prole, C.W. Taylor, Ca2+ signals initiate at immobile IP3 receptors adjacent to ER-plasma membrane junctions, Nat. Commun. 8 (2017) 1505, https://doi.org/10.1038/s41467-017-01644-8.
[10] M.D. Bootman, M.J. Berridge, P. Lipp, Cooking with Calcium: the Recipes for Composing Global Signals from Elementary Events, Cell 91 (1997) 367–373, https://doi.org/10.1016/S0092-8674(00)80420-1.
[11] M.J. Berridge, Elementary and global aspects of calcium signalling, J. Physiol. 499 (1997) 291–306, https://doi.org/10.1113/jphysiol.1997.sp021927.
[12] M.D. Bootman, M.J. Berridge, Subcellular Ca2+ signals underlying waves and graded responses in HeLa cells, Curr. Biol. 6 (1996) 855–865, https://doi.org/10.1016/S0960-9822(02)00609-7.
[13] J.S. Marchant, I. Parker, Role of elementary Ca2+ puffs in generating repetitive Ca2+ oscillations, EMBO J 20 (2001) 65–76.
[14] J. Marchant, N. Callamaras, I. Parker, Initiation of IP3-mediated Ca2+ waves in Xenopus oocytes, EMBO J 18 (1999) 5285–5299, https://doi.org/10.1093/emboj/18.19.5285.
[15] S. Mataragka, C.W. Taylor, All three IP3 receptor subtypes generate Ca2+ puffs, the universal building blocks of IP3-evoked Ca2+ signals, J. Cell Sci. (2018). 10.1242/jcs.220848.
[16] J.T. Lock, I. Parker, IP3 mediated global Ca2+ signals arise through two temporally and spatially distinct modes of Ca2+ release, Elife 9 (2020) e55008, https://doi.org/10.7554/eLife.55008.
[17] J. Suzuki, K. Kanemaru, K. Ishii, M. Ohkura, Y. Okubo, M. Iino, Imaging intraorganellar Ca2+ at subcellular resolution using CEPIA, Nat. Commun. 5 (2014) 4153, https://doi.org/10.1038/ncomms5153.
[18] K.L. Ellefsen, B. Settle, I. Parker, I.F. Smith, An algorithm for automated detection, localization and measurement of local calcium signals from camera-based imaging, Cell Calcium 56 (2014) 147–156, https://doi.org/10.1016/j.ceca.2014.06.003.
[19] K.L. Ellefsen, J.T. Lock, B. Settle, C.A. Karsten, I. Parker, Applications of FLIKA, a Python-based image processing and analysis platform, for studying local events of cellular calcium signaling, Biochim. Biophys. Acta - Mol. Cell Res. 1866 (2019) 1171–1179, https://doi.org/10.1016/j.bbamcr.2018.11.012.
[20] J.T. Lock, K.J. Alzayady, D.I. Yule, I. Parker, All three IP3 receptor isoforms generate Ca2+ puffs that display similar characteristics, Sci. Signal. 11 (2018) eaau0344, https://doi.org/10.1126/scisignal.aau0344.
[21] G.D. Dickinson, D. Swaminathan, I. Parker, The Probability of Triggering Calcium Puffs Is Linearly Related to the Number of Inositol Trisphosphate Receptors in a Cluster, Biophys. J. 102 (2012) 1826–1836, https://doi.org/10.1016/j.bpj.2012.03.029.
[22] I.F. Smith, I. Parker, Imaging the quantal substructure of single IP3R channel activity during Ca2+ puffs in intact mammalian cells, Proc. Natl. Acad. Sci. U. S. A. 106 (2009) 6404–6409, https://doi.org/10.1073/pnas.0810799106.
[23] M. Bootman, E. Niggli, M. Berridge, P. Lipp, Imaging the hierarchical Ca2+ signalling system in HeLa cells, J. Physiol. 499 (1997) 307–314. http://www.ncbi.nlm.nih.gov/pmc/articles/PMC1159306/.
[24] N. Callamaras, J.S. Marchant, X.-.P. Sun, I. Parker, Activation and co-ordination of InsP3-mediated elementary Ca2+ events during global Ca2+ signals in Xenopus oocytes, J. Physiol. 509 (1998) 81–91, https://doi.org/10.1111/j.1469-7793.1998.081bo.x.
[27] S.L. Dargan, I. Parker, Buffer kinetics shape the spatiotemporal patterns of IP3-evoked Ca2+ signals, J. Physiol. 553 (2003) 775–788, https://doi.org/10.1113/jphysiol.2003.054247.
[28] S.L. Dargan, B. Schwaller, I. Parker, Spatiotemporal patterning of IP3-mediated Ca2+ signals in Xenopus oocytes by Ca2+-binding proteins, J. Physiol. 556 (2004) 447–461, https://doi.org/10.1113/jphysiol.2003.059204.
[29] I.F. Smith, S.M. Wiltgen, I. Parker, Localization of puff sites adjacent to the plasma membrane: functional and spatial characterization of Ca2+ signaling in SH-SY5Y cells utilizing membrane-permeant caged IP3, Cell Calcium 45 (2009) 65–76, https://doi.org/10.1016/j.ceca.2008.06.001.
[30] I.F. Smith, S.M. Wiltgen, J. Shuai, I. Parker, Ca2+ puffs originate from preestablished stable clusters of inositol trisphosphate receptors, Sci. Signal. 2 (2009) ra77, https://doi.org/10.1126/scisignal.2000466. LP-ra77.
[31] K.L. Ellefsen, J.T. Lock, B. Settle, C.A. Karsten, I. Parker, Applications of FLIKA, a Python-based image processing and analysis platform, for studying local events of cellular calcium signaling, Biochim. Biophys. Acta - Mol. Cell Res. 1866 (2019), https://doi.org/10.1016/j.bbamcr.2018.11.012.
[32] I. Parker, I. Ivorra, Localized all-or none calcium liberation by inositol trisphosphate, Science (80-.) 250 (1990) 977–979. http://science.sciencemag.org/content/250/4983/977.abstract.
[33] I. Parker, I.F. Smith, Recording single-channel activity of inositol trisphosphate receptors in intact cells with a microscope, not a patch clamp, J. Gen. Physiol. 136 (2010) 119–127, https://doi.org/10.1085/jgp.200910390.
[34] S.M. Wiltgen, I.F. Smith, I. Parker, Superresolution localization of single functional IP3R channels utilizing Ca2+ flux as a readout, Biophys. J. 99 (2010) 437–446, https://doi.org/10.1016/j.bpj.2010.04.037.
[35] D.-O.D. Mak, J.K. Foskett, Inositol 1,4,5-trisphosphate receptors in the endoplasmic reticulum: a single-channel point of view, Cell Calcium 58 (2015) 67–78, https://doi.org/10.1016/j.ceca.2014.12.008.
[36] K.L. Ellefsen, I. Parker, Dynamic Ca2+ imaging with a simplified lattice light-sheet microscope: a sideways view of subcellular Ca2+ puffs, Cell Calcium 71 (2018) 34–44, https://doi.org/10.1016/j.ceca.2017.11.005.
[37] L. Birnbaumer, X. Zhu, M. Jiang, G. Boulay, M. Peyton, B. Vannier, D. Brown, D. Platano, H. Sadeghi, E. Stefani, M. Birnbaumer, On the molecular basis and regulation of cellular capacitative calcium entry: roles for Trp proteins, Proc. Natl. Acad. Sci. 93 (1996) 15195, https://doi.org/10.1073/pnas.93.26.15195. LP –15202.

[38] E.A. Matthews, D. Dietrich, Buffer mobility and the regulation of neuronal calcium domains, Front. Cell. Neurosci. 9 (2015) 48, https://doi.org/10.3389/fncel.2015.00048.
[39] K. Dakin, W.-.H. Li, Cell membrane permeable esters of D-myo-inositol 1,4,5-trisphosphate, Cell Calcium 42 (2007) 291–301, https://doi.org/10.1016/j.ceca.2006.12.003.
[40] R. Thul, M. Falcke, Release Currents of IP3 Receptor Channel Clusters and Concentration Profiles, Biophys. J. 86 (2004) 2660–2673, https://doi.org/10.1016/S0006-3495(04)74322-2.
[41] M. Yamasaki-Mann, I. Parker, Enhanced ER Ca2+ store filling by overexpression of SERCA2b promotes IP3-evoked puffs, Cell Calcium 50 (2011) 36–41, https://doi.org/10.1016/j.ceca.2011.04.008.
[42] R. Caroppo, M. Colella, A. Colasuonno, A. DeLuisi, L. Debellis, S. Curci, A.M. Hofer, A Reassessment of the Effects of Luminal [Ca2+] on Inositol 1,4,5-Trisphosphate-induced Ca2+ Release from Internal Stores, J. Biol. Chem. 278 (2003) 39503–39508, https://doi.org/10.1074/jbc.M305823200.
[43] M. Yamasaki-Mann, A. Demuro, I. Parker, Cytosolic [Ca2+] regulation of InsP3-evoked puffs, Biochem. J. 449 (2013) 167, https://doi.org/10.1042/BJ20121271. LP –173.
[44] H. Vais, J.K. Foskett, G. Ullah, J.E. Pearson, D.-.O. Daniel Mak, Permeant calcium ion feed-through regulation of single inositol 1,4,5-trisphosphate receptor channel gating, J. Gen. Physiol. 140 (2012) 697–716, https://doi.org/10.1085/jgp.201210804.
[45] H. Vais, M. Wang, K. Mallilankaraman, R. Payne, C. McKennan, J.T. Lock, L. A. Spruce, C. Fiest, M.Y. Chan, I. Parker, S.H. Seeholzer, J.K. Foskett, D.-O.D. Mak, ER-luminal [Ca2+] regulation of InsP3 receptor gating mediated by an ER-luminal peripheral Ca2+-binding protein, Elife 9 (2020) e53531, https://doi.org/10.7554/eLife.53531.
[46] S.M. Emrich, R.E. Yoast, P. Xin, V. Arige, L.E. Wagner, N. Hempel, D.L. Gill, J. Sneyd, D.I. Yule, M. Trebak, Omnitemporal choreographies of all five STIM/Orai and IP3Rs underlie the complexity of mammalian Ca2+ signaling, Cell Rep 34 (2021), https://doi.org/10.1016/j.celrep.2021.108760.
[47] M. Prakriya, R.S. Lewis, Store-Operated Calcium Channels, Physiol. Rev. 95 (2015) 1383–1436, https://doi.org/10.1152/physrev.00020.2014.